Mechanistic Insights into Nanostructure Formation via Phase-Field Modeling and Experimental Validation of Metal-Assisted Chemical Etching

Kun-Dar Li* and David T.W. Lin*

Keywords：metal-assisted chemical etching, phase-field modeling, nanostructure fabrication surface morphology, numerical simulation

ABSTRACT

Metal-assisted chemical etching (MACE) is crucial for modifying semiconductor surface morphology, especially in fabricating extremely high aspect ratio structures for silicon. This study combines phase-field modeling and experiments to explore MACE mechanisms. Numerical simulations show that metal catalyst characteristics, especially particle size, significantly affect surface evolution. Larger particles create deeper cavities and rougher surfaces while maintaining etching rates. Particle distribution patterns have minimal impact. Experiments with Au-coated GaAs substrates validate the model, showing strong agreement between simulations and actual morphologies. Under the conditions of high oxidant concentrations, the etching reactions and surface morphological features are enhanced due to the accelerated rate of chemical reactions. This work provides a computational framework for optimizing MACE, offering insights for nanoelectronics, photovoltaics, and sensors. The phase-field modeling approach is a powerful tool for nanoscale surface engineering.

INTRODUCTION

In recent years, metal-assisted chemical etching (MACE) has emerged as a significant technique for developing intricate nanostructures on semiconductors and other substrates. This innovative method leverages the catalytic properties of metals, typically deposited on a substrate, to selectively accelerate the chemical etching process. The unique etching process plays a crucial role in various fields, from nanoelectronics to optoelectronics, as it enables precise control over surface morphologies and facilitates the fabrication of structures at the nanoscale (Stafiniak et al., 2018; Jiang et al., 2016; Li et al., 2015; Geng et al., 2012; Wu and Cui, 2012). The MACE method offers several advantages over traditional nanofabrication techniques, making it a compelling choice for various applications in semiconductor manufacturing and nanostructure development. For instance, MACE allows for anisotropic etching, meaning it can create structures with steep sidewalls, which is often required in semiconductor applications (Celik et al., 2022). Unlike isotropic wet etching methods that attack the substrate uniformly, MACE can selectively etch in specific directions based on the placement of metal catalysts, leading to more precise control over the final geometry of the etched features. Compared to gas-phase etching techniques like reactive ion etching (RIE), which require expensive equipment and complex setups, MACE is relatively inexpensive. It utilizes simple wet chemistry processes, making it more accessible for research and industrial applications (Arafat et al., 2021). MACE can also be integrated with conventional lithography techniques, allowing for the selective deposition of metal catalysts on desired areas of a substrate. This compatibility enhances its utility in creating complex nanostructures while leveraging existing fabrication infrastructure (Kolasinski, 2021).

In applications like solar cell manufacturing, MACE can create micro- or nanotextured surfaces that significantly improve light trapping efficiency (Liu et al., 2022; He et al., 2013; Zhang et al., 2019). This feature is crucial for enhancing the performance of photovoltaic devices by increasing their absorption capabilities. The technique allows for fine control over the morphology of nanostructures, including the size and shape of features created on the substrate. This capability is essential for tailoring materials to meet specific performance criteria in various applications, such as sensors and electronic devices (Kolasinski et al., 2019; Dusheiko et al., 2022; Mohamedyaseen and Suresh, 2022; Lin et al., 2023). As a consequence,

Paper Received April, 2025. Revised May, 2025. Accepted June, 2025. Author for Correspondence: David T.W. Lin.

** Professor, Department of Materials Science, National University of Tainan, Tainan, Taiwan 70005, ROC.*

understanding the mechanisms of MACE is essential for optimizing the etching parameters and achieving desired structural outcomes. Due to the complexity, fully understanding the interplay between redox reactions, charge transfer, and mass transport is still ongoing (Nur'aini and Oh, 2022; Leonardi et al., 2021). The theoretical modeling of MACE includes detailed exploration of vacancy generation, diffusion, and pore formation on the substrate during the reaction (Kolasinski, 2021). The interaction of factors such as the metal type, particle size, and distribution affect the rate and pattern of etching. By examining the reaction kinetics and vacancy dynamics, various etching conditions influence surface morphology can be simulated and predicted. The insights from the theoretical models are critical for enhancing the efficiency and precision of MACE, ultimately aiding in the design and application of nanostructured devices (Salem et al., 2020). In this study, a comprehensive theoretical model is introduced to simulate MACE processes, examining the influence of variables such as particle size, distribution, and etching parameters on surface evolution. The phase-field model applied here facilitate the simulation of structural evolutions, providing valuable insights into the controlled creation of nanoscale features. This study work also includes experimental validation to assess model accuracy and its alignment with observed surface morphologies under varied etching conditions.

THEORETICAL MODEL

Regarding to the mechanisms of metal-assisted chemical etching (MACE) (Kong et al., 2016), several critical steps are involved. First, the oxidant is preferentially reduced at the metal surface due to the pronounced catalytic activity of the metal. As the oxidant is reduced, electron holes are transferred from the metal and subsequently introduced into the substrate. Following this, the substrate atoms are oxidized by these electron holes and dissolved by the etchant at the interface between the metal and substrate. The substrate regions in contact with the metal are etched more rapidly than bare substrate surface exposed only to the etchant. To develop a theoretical model for MACE based on these related processes, it is assumed that vacancies are generated in the substrate during the chemical etching reaction. As the etching reactants is uniformly distributed across the entire substrate surface and continue to interact with it, vacancies are consistently introduced into the substrate throughout the etching progress. As the vacancy concentration in the substrate increases, the free energy of the substrate raises, leading to a decrease in system stability. To minimize the free energy and move toward thermodynamic equilibrium, the vacancies segregate and form pores, resulting in the development of a characteristic microstructure in the substrate. In this study, the diffusion equation of vacancy is employed to describe the structural evolution of substrate during the MACE process, as follows:

$$\frac{\partial C_v}{\partial t} = \nabla \cdot \left(\frac{M}{N^2} \nabla \left(\frac{\partial G}{\partial C_v} \right) \right) + \varepsilon_{chemical} + \varepsilon_{MACE} \quad (1)$$

where C_v represents the vacancy concentration in the substrate, t is the time, M is the vacancy mobility, N is the number of atomic sites per unit volume, G represents the total free energy of the substrate, $\varepsilon_{chemical}$ and ε_{MACE} are the etching rates for the regular chemical reaction and MACE, respectively. Several factors can influence the rate of $\varepsilon_{chemical}$, including the chemical reaction mechanism and process conditions. For isotropic chemical etching reaction, $\varepsilon_{chemical}$ remains constant. However, when considering a crystalline substrate or anisotropic chemical etching, an anisotropic function is incorporated into $\varepsilon_{chemical}$. ε_{MACE} is governed by the metal-assisted chemical etching reaction mechanism and its associated process conditions. The vacancy concentration (C_v) in the substrate ranges from 0 to 1. As C_v approaches 1, a high vacancy concentration signifies a pseudo-vacancy phase. Conversely, when C_v is close to 0, an extremely low vacancy concentration corresponds to the substrate phase. In Equation (1), the total free energy G of the substrate system is comprised of both the mixing free energy and the interfacial energy, as described (Kobayashi, 1993; Eggleston et al., 2001; Kim, 2007; Cahn and Hilliard, 1958):

$$G = \int_V \left[g(C_v) + \frac{r^2}{2} |\nabla C_v|^2 \right] dv \quad (2)$$

where $g(C_v)$ denotes the mixing free energy of atoms and the vacancies in the substrate, γ represents the interfacial energy coefficient, and v is the total system volume. In this model, the mixing free energy in the substrate can be characterized by $g(C_v) = g_v C_v + g_a(1 - C_v) + Nk_B T[C_v ln C_v + (1 - C_v)\, ln\, (1 - C_v)\,] + N\Omega C_v(1 - C_v)$ with the free energy of vacancies per unit volume (g_v), the free energy of the substrate per unit volume (g_a), Boltzmann constant (k_B), the absolute temperature (T) and the parameter of interatomic bond energy (Ω). For an amorphous substrate, the interfacial energy is isotropic, and γ can be treated as a constant. However, when a specific crystal substrate is considered, the interfacial energy becomes a spatial function, and anisotropic diffusion must also be accounted for. In this study, an isotropic case is initially adopted.

With respect to the etching reaction, $\varepsilon_{chemical}$ and ε_{MACE} are expressed as,

$$\varepsilon_{chemical} = \varepsilon_c^0 \cdot |\nabla C_v|^2 \quad (3)$$

where ε_c^0 represents the chemical etching rate, which depends on the reaction rates between the etchant and solid atoms. For a crystalline matrix, ε_c^0 can also be a function of the crystallographic orientation. Similarly,

$$\varepsilon_{MACE} = \varepsilon_M^0 \cdot |\nabla C_M|^2 \cdot |\nabla C_V|^2 \quad (4)$$

where ε_M^0 is the etching rate of the MACE reaction, and C_M denotes the concentration of the metal phase.

To perform the numerical simulation of the MACE process based on Eq. (1), the length scale is defined as $l_0 = \gamma \cdot (Nk_BT)^{-1/2}$, and the time scale is given by $\tau = (\gamma/k_BT)^2/M$, respectively. Eq. (1) is then normalized using l_0 and τ to derive a dimensionless equation for an isotropic system, expressed as:

$$\frac{\partial C_v}{\partial t^*} = \nabla^2\left(\frac{g^*(C_v)}{C_v} - \nabla^2 C_v\right) + \varepsilon^*_{chemical} + \varepsilon^*_{MACE} \quad (5)$$

where t^* is the normalized time, ∇^2 is the normalized Laplace operator, $g^*(C_v) = g(C_v)/Nk_BT$, $\varepsilon^*_{chemical} = l_0\tau\varepsilon_{chemical}$, and $\varepsilon^*_{MACE} = l_0\tau\varepsilon_{MACE}$.

Based on the governing equation presented in Eq. (5), a series of numerical simulations for the MACE process was conducted. Additionally, the impact of various etching process parameters on the formation and evolution of surface morphologies was also investigated. The finite volume method was employed to perform the numerical simulations for a three-dimensional theoretical model. In this study, the grid size for the numerical calculations was set at 60×60×60 to simulate surface morphologies under different MACE conditions. The grid spacing was 0.5, with a time step of 0.5. To replicate experimental etching conditions, the rational simulation parameters were derived from literatures or relevant experimental values, including $N{\sim}1\times10^{19}m^{-2}$, $\gamma^2{\sim}8\times10^{-19}J$, $\Omega/k_BT{\sim}3.75$ (Cahn and Hilliard, 1958; Yu and Lu, 2005; Suo and Lu, 2000). Other process parameters, such as particle size, quantity and the distribution of metals, were also examined and discussed for their effects on the formation and evolution of etched surface morphologies. Furthermore, the depths of the metal-assisted etching and chemical etching were individually calculated based on the simulation results to quantitatively characterize the features of the etching process. In this study, the vacancy concentration (C_v) is initialized with a Gaussian function centered at the top of the substrate to represent a free surface. In addition, a second field variable, the metal concentration (C_M), is introduced, with a spherical shape initially positioned on the substrate surface. The formula for the spherical metal field variable is expressed as follows:

$$C_M^i = exp\left[-\frac{(x-x_i)^2 + (y-y_i)^2 + (z-z_i)^2}{2\sigma_i}\right] \quad (6)$$

where σ_i is the standard deviation parameter, defined as $r_i^2/(-2ln(0.5))$, and $(x_i,\ y_i,\ z_i)$ represents the randomly generated coordinates of the *i*-th metallic particle's center. The z_i coordinate will be recalculated at each step of the simulation based on the position of the substrate surface.

RESULTS AND DISCUSSION

Figure 1 illustrates a typical simulation result of structural formation calculated by this model, featuring a ratio of $R_\varepsilon = \varepsilon^*_{MACE}/\varepsilon^*_{chemical}$ =30, $\varepsilon^*_{chemical}$ =0.02 and the metal particle radius of 5.3125nm during the metal-assisted chemical etching (MACE) process. In the figure, the dark regions represent the substrate, while the orange particles indicate the catalytic metals. As shown in Fig. 1(a), the metal particles are randomly distributed on the substrate surface as the initial condition in this simulation. During the early stages of the etching process, shallow pits form around the metal particles due to the metal-assisted etching reaction, as seen in Fig. 1(b). Since the surface of the substrate is simultaneously subjected to chemical etching and metal-assisted etching, the effect of chemical etching can be observed by comparing the surface depth differences between Figs. 1 (a) and (b). As the etching reactions progress, the significantly faster metal-assisted etching rate causes the metal particles to gradually sink into the substrate, as depicted in Fig. 1(c). Furthermore, with only five isolated metal particles considered in this simulation, individual etch caves develop over time, as shown in Fig. 1(d). This figure also reveals that the diameter of the etch caves is slightly wider at the top than at the bottom, attributed to the longer exposure time of the substrate surface to the chemical etchants. This simulation results align closely with the experimental observations of MACE, demonstrating the model's capability to accurately replicate the mechanisms and surface characteristics of the process. To further investigate the detailed effects of catalytic metals on the etching process, various conditions of the catalytic metals, including the particle size, quantity and distribution, are incorporated into subsequent numerical simulations.

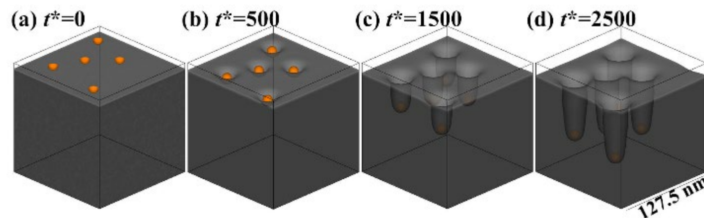

Fig. 1. Simulation results of structural formation during the MACE process using the phase-field model. t^* is the simulation time.

Next, two different sizes of the metal particles are evaluated by setting the metal particle radii as 4.25nm and 6.375nm, respectively, while keeping all other numerical parameters consistent with those used in Fig. 1. The simulation results of MACE with different particle size are shown in Fig. 2, with quantitative analyses of the etched surface morphologies presented in Fig. 3. Figs. 2(a)-(c) illustrate the MACE process with smaller particles, while Figs. 2(d)-(f) depict the surface evolution with larger particles. In both cases, similar surface etching behavior is observed from the initial to later stages of the process. At the early stage, the randomly distributed metal particles form tiny etch pits, as shown in Figs. 2(a) and 2(d). Over time, the catalytic effect of the metal particles gradually produces surface cavities around their locations, and the removal of surface atoms causes the top surface to move downward. Two distinct etching depths are revealed on the surface, corresponding to the behaviors of metal-assisted etching and chemical etching. The primary difference between the two particle sizes lies in the etched depths created by the catalytic metals. For smaller particles, shallow cavities are observed, as seen in Fig. 2(c), while larger particles produce deeper etching holes, as shown in Fig. 2(f). This difference can be attributed to the larger surface area of contact between the catalytic metal and the substrate for larger particles, leading to a higher etching rate. However, the chemical etching rates for both particle sizes are nearly identical, resulting in similar top-surface etching depths, as seen in Figs. 2(b)-(c) and Figs. 2(d)-(f). It is also noteworthy that when randomly distributed metal particles are positioned too closely, the etched pits may merge to form larger cavities. The impact of these merged cavities on the etching rate and surface morphology will be discussed further in a later section.

The qualitative descriptions of the influence of particle size in Fig. 2 are supported by the quantitative analysis of surface morphologies shown in Fig. 3. In Fig. 3(a), the depths of the metal-assisted etching and the chemical etching over time are presented for the case with smaller particle size. From the slopes of the curves, the etching rates are calculated as 0.0205 and 0.0031, respectively. This indicates that the metal-assisted etching rate is approximately 6.6 times higher than the chemical etching rate in this simulation. For the case with larger particle size, shown in Fig. 3(b), the metal-assisted etching and chemical etching rates are determined as 0.037 and 0.0029, respectively. The results reveal that the rate of the metal-assisted etching increases with particle size, while the chemical etching rate remains largely unaffected. The surface roughness measurements in Fig. 3(c) further illustrate the effect of particle size on surface features. Larger metal particles result in higher surface roughness, consistent with the observations from the experimental results (Shimizu et al., 2016).

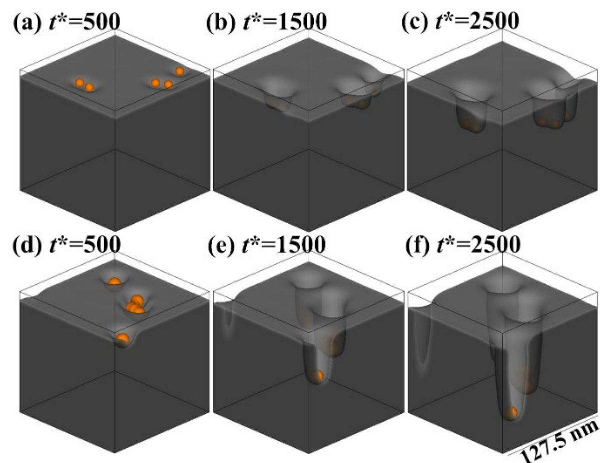

Fig. 2. Simulation results of MACE with varying particle sizes: (a)-(c) particle radius = 4.25nm, and (d)-(f) particle radius = 6.375nm.

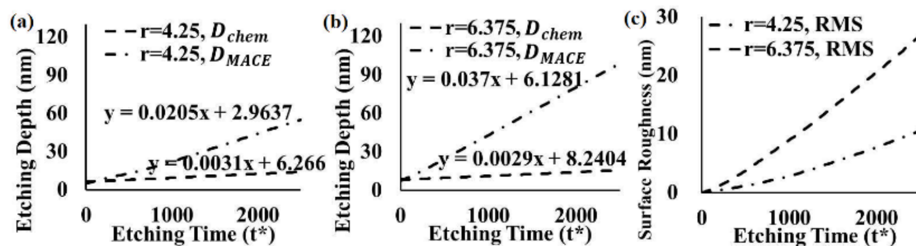

Fig. 3. Quantitative analysis of surface morphologies: (a) depths of etched surface for particle radius = 4.25nm, (b) depths of etched surface for particle radius = 6.375nm, and (c) surface roughness. D_{chem} represents depths from chemical etching, D_{MACE} represents depths from metal-assisted etching, and RMS indicates root-mean-square roughness.

To investigate the influence of the combination of etching holes and the quantity of metal particles on the MACE process, five and ten randomly distributed metal particles with a radius of 6.375nm are applied to the surface as the initial condition for the simulation. All other parameters remain consistent with those used in Fig. 1. Fig. 4(a) demonstrates that five distinct etch pits form individually during the early stage of the etching process. As the etching continues, cone-shaped etched holes develop. On the top surface, some sections of the sidewalls between the etch pits are etched away, leading to the merging of adjacent pits,

as illustrated in Figs. 4(b) and 4(c). When ten metal particles are considered, their closer proximity increases the likelihood of contact between particles. As shown in Fig. 4(d), the particles tend to cluster or form bands. Compared to Fig. 4(a), a cluster of the metal particles is more likely to create a larger, irregularly shaped etch pit in the initial stage of the process. Over time, groove-like etched patterns emerge on the substrate surface, with granular metals located at the bottoms of the etch pits at uneven depths, as depicted in Figs. 4(e) and 4(f). Quantitative analysis of these simulations, shown in Figs. 5(a) and 5(b), reveals that the slopes of the depth curves for metal-assisted etching with five and ten particles are 0.0324 and 0.0301, respectively. Similarly, the slopes for chemical etching are nearly identical, at 0.003 and 0.0028, regardless of the number of particles. These results demonstrate that the number of metal particles has minimal impact on the etching process. Only a slight difference in the surface roughness is observed in Fig. 5(c), with a slightly rougher surface attributed to the relatively larger number of metal particles.

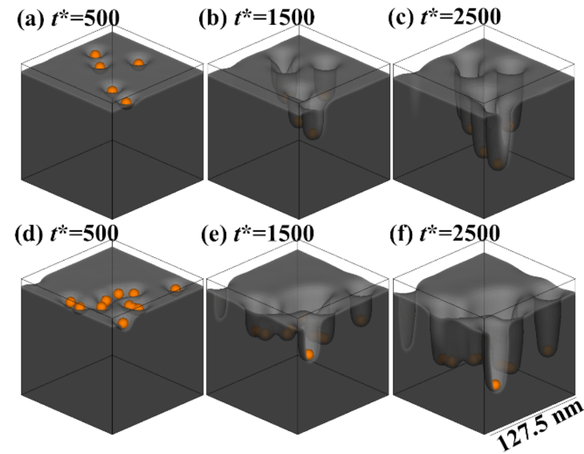

Fig. 4. Simulation results of MACE with varying particle quantities: (a)-(c) five randomly distributed particles, and (d)-(f) ten randomly distributed particles.

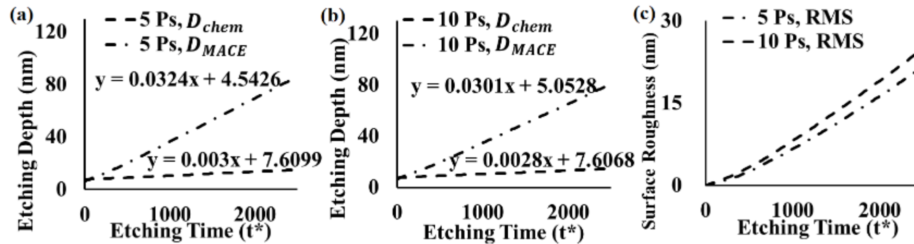

Fig. 5. Quantitative analysis of surface morphologies: (a) depths of etched surface with five particles, (b) depths of etched surface with ten particles, and (c) surface roughness.

For applications in various novel devices, such as field-emission displays, nanoelectronics, and nanophotonic, an ordered pattern of the etched structures is desirable to enhance electronic and magnetic properties (Huang et al., 2007; DeJarld et al., 2011). In this study, a periodic distribution of the metal particles is incorporated into the numerical simulation to investigate the surface evolution during MACE. Additionally, different particle sizes with a periodic distribution are considered in the simulations to further examine their combined influence on the surface morphology. Figs. 6(a)-(c) and 6(d)-(f) present the simulation results for periodic distributions with particle radii of 4.25nm and 6.375nm, respectively. Quantitative analyses of the etched surfaces are shown in Fig. 7. At the initial stage of etching, periodic shallow pits are observed at the positions of metal particles, as shown in Figs. 6(a) and 6(d). As the etched process continues, the surface morphology of the substrate with small metal particles evolves from shallow pits to vertical pits, resembling a honeycomb porous structure, as depicted in Figs. 6(b) and 6(c). In contrast, for larger metal particles, the sidewalls of the etch pit are eventually etched away, resulting in the formation of vertical columnar structures in the later stages, as demonstrated in Figs. 6(d) and 6(f). Both metal-assisted etching and the chemical etching play crucial roles in creating these nano-columnar features. Quantitative analysis in Fig. 7 reveals that the etching depth curves for periodic distributions closely match those for random distributions of metal particles in Fig. 3. For instance, the slopes of the depth curves for metal-assisted etching with small particles are 0.0205 and 0.0219 for random and periodical distributions, respectively, as seen in Fig. 3(a) and Fig. 7(a). Similarly, for large particles, the slopes are 0.037 and 0.0374, respectively, as shown in Fig. 3(b) and Fig. 7(b). These results indicate that the particle distribution pattern has minimal influence on the etching rate, which is primarily determined by particle size. Surface roughness analysis in Fig. 7(c) highlights that periodic distributions produce higher surface roughness, especially with vertical columnar structures, compared to random distributions. This is corroborated by the slopes of the surface roughness curves in Figs. 3(c) and 7(c), showing that periodic particle distributions result in greater roughness. This difference may arise because individual etched holes are more distinctly formed in periodic distributions, whereas in random distributions, some etched pits merge, leading to a slight reduction in surface roughness.

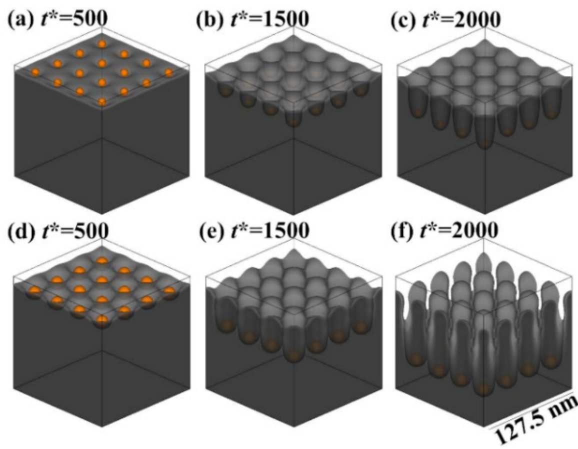

Fig. 6. Simulation results of MACE with periodic particle distributions: (a)-(c) particle radius = 4.25nm, and (d)-(f) particle radius = 6.375nm.

To further study the impact of varying etching rates on the MACE with a periodical particle distribution, different ratios ($R_\varepsilon = \varepsilon^*_{MACE}/\varepsilon^*_{chemical}$) of 20 and 40 are evaluated to represent various levels of the MACE conditions. The simulation results for etched surface evolution are shown in Figs. 8(a)-(c) and 8(d)-(f), corresponding to low and high metal-assisted chemical etching effects, respectively. In Fig. 8(a), with R_ε=20, the periodical metal particles are distributed in shallow pits. Under low metal-assisted chemical etching conditions, the surface morphology evolves from shallow pits to vertical etch pits, as seen in Figs. 8(b) and 8(c). A cross-section view in Fig. 8(c) reveals U-shaped structures at the bottom of the vertical etch pits, while the top of the substrate exhibits a wavy, bumpy texture due to the periodicity of the etch pits. When R_ε is increased to 40, the development of vertical etch pits is significantly accelerated, as shown in Figs. 8(d) and 8(e). Compared to Fig. 8(c), elongated etch pits form under high metal-assisted chemical etching conditions. After a period of the chemical etching, the sidewalls of the etch pits are etched away, leaving columnar structures, as shown in Fig. 8(f).

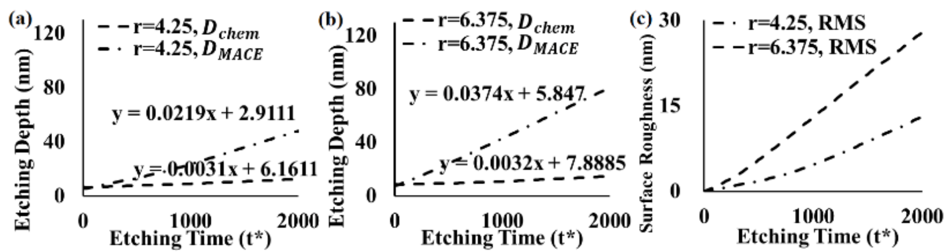

Fig. 7. Quantitative analysis of surface morphologies with periodic particle distributions: (a) depths of etched surface for particle radius = 4.25nm, (b) depths of etched surface for particle radius = 6.375nm, and (c) surface roughness.

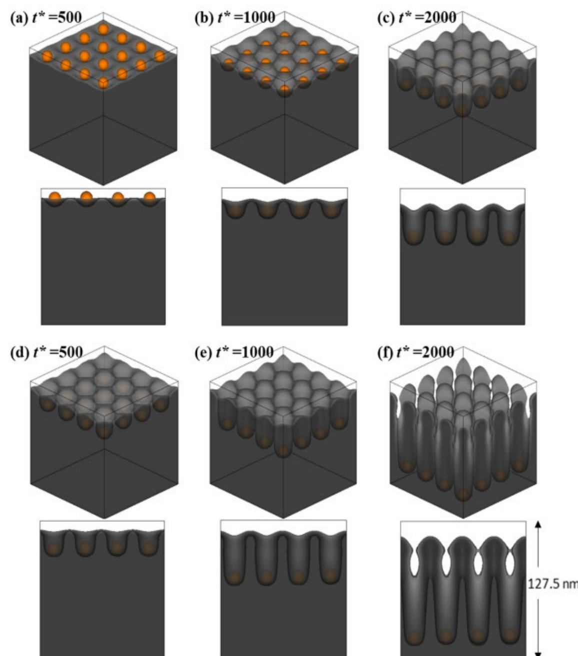

Fig. 8. Simulation results of MACE with periodic particle distributions: (a)-(c) R_ε = 20, and (d)-(f) R_ε = 40.

Quantitative analysis in Figs. 9(a) and 9(b) indicates that the etching rates for R_ε=20 and 40 are 0.0291 and 0.0616, respectively. The ratio of these etching rates, approximately 2.1, aligns closely with the value of R_ε. This indicates that the effect of MACE is primarily governed by the parameter of R_ε, which directly affects the etching rate. In Fig. 9(c), the slopes of the surface roughness for the two MACE conditions are 0.0075 and 0.0214, respectively. A higher metal-assisted chemical etching rate results in higher surface roughness, consistent with the formation of columnar morphologies.

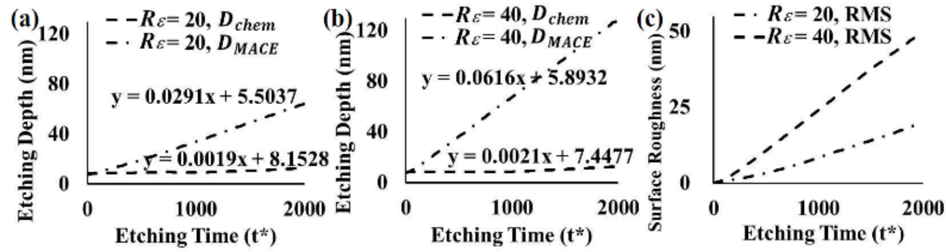

Fig. 9. Quantitative analysis of surface morphologies with periodic particle distributions: (a) the depths of etched surface with R_ε = 20, (b) the depths of etched surface with R_ε = 40, and (c) surface roughness.

In this study, validation experiments on metal-assisted chemical etching (MACE) were conducted using an Au-coated GaAs substrate. The substrate was etched with a mixture of sulfuric acid and potassium permanganate at 40°C. Two different concentrations of potassium permanganate, 0.01wt% and 0.1wt%, were used to simulate various conditions of the MACE process. For comparison, additional numerical simulations were performed with low and high chemical etching effects in random distributions of metal particles. Figs. 10(a)-(c) and 10(d)-(f) illustrate the simulation results for two scenarios: low chemical etching with high metal-assisted etching effects ($\varepsilon^*_{chemical}$ =0.003 and R_ε=40), and high chemical etching with low metal-assisted etching effects ($\varepsilon^*_{chemical}$=0.006 and R_ε=20), respectively. In Fig. 10(a), etched pits appear at the positions of the distributed metals. The depths of the etched pits increase over time, as shown in Fig. 10(b). In addition to the vertical etch cavities produced by the metal-assisted etching, tiny holes etched by the chemical etching begin to appear on the remaining surface, as presented in Fig. 10(c). When the chemical etching rate ($\varepsilon^*_{chemical}$) is doubled, most of the tiny bumps induced by the chemical etching form earlier on the substrate surface, as shown in Fig. 10(d). With the intensified chemical etching effect, the average surface position of the etched substrate becomes lower, and the surface morphology becomes rougher, as exhibited in Figs. 10(e) and (f). Figs. 11(a) and (b) show the quantitative measurements of the metal-assisted etching depths and the chemical etching depths for different chemical etching conditions in the simulations. These analytical values are consistent with the qualitative observations and align with the numerical parameter settings. The slopes of the chemical etching rate are 0.0002 and 0.0066, respectively, for low and high chemical etching effects. Moreover, the almost identical slopes of the metal-assisted etching rate are calculated as 0.0622 and 0.0662, respectively, in these two simulations. For the surface roughness analysis in Fig. 11(c), the two curves of the surface roughness nearly overlap in these simulations. Comparing with the experiments of the metal-assisted chemical etching with different potassium permanganate concentrations, Fig. 10(g) presents a featured surface morphology of an Au-coated GaAs substrate etched with sulfuric acid and low potassium permanganate (0.01wt%) for 10 minutes. The characteristics of the etched surface fit well with the numerical simulation, including the deep pits and the shallow bumps on the surface due to the metal-assisted and chemical etching. Potassium permanganate acts as an oxidant in the etching process. As the concentration of the oxidant increases, the etching reaction accelerates. For a high concentration of potassium permanganate (0.1wt%), the effect of the chemical etching is enhanced, which can be observed by the enlarged bumps alongside the metal-assisted etching pits, as shown in Fig. 10(h). However, it should be noticed that the excessive oxidant concentrations can destabilize the Au, leading to nonuniform etching and structural defects. The similarities between experimental and simulated surface features validate the numerical model, although further experimental efforts are required to refine the simulation parameters.

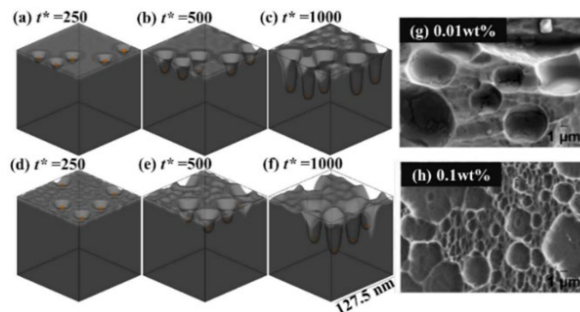

Fig. 10. Simulation results of MACE: (a)-(c) ε^*_{chem} = 0.003 and R_ε = 40, (d)-(f) ε^*_{chem} = 0.006 and R_ε =20. Validation experiments with an Au-coated GaAs substrate etched by sulfuric acid mixed with varying concentrations of potassium permanganate at 40°C: (g) 0.01wt%, and (h) 0.1wt%.

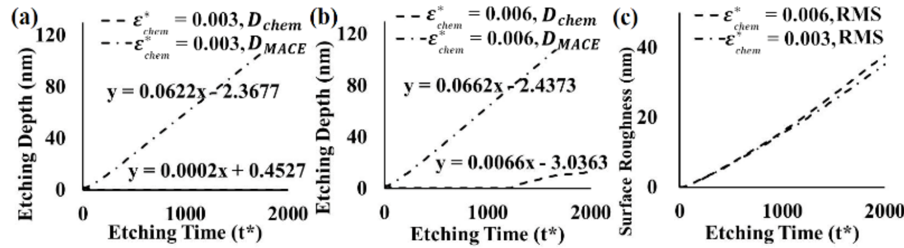

Fig. 11. Quantitative analysis of surface morphologies with random particle distributions: (a) the depths of etched surface with ε^*_{chem} = 0.003 and R_ε = 40, (b) the depths of etched surface with ε^*_{chem} = 0.006 and R_ε = 20, and (c) surface roughness.

CONCLUSIONS

Metal-assisted chemical etching (MACE) is a versatile nanofabrication technique with immense potential for precise surface morphology modification across various technological fields. This study explores the intricate mechanisms of MACE through an innovative combination of phase-field modeling and experimental validation. The numerical simulations revealed critical insights into the etching process, highlighting the interplay between metal catalysts, chemical etching rates, and substrate structural evolution. Key findings demonstrate that metal particle characteristics, such as size, distribution, and quantity, significantly influence surface morphologies. Larger metal particles were shown to produce deeper etching cavities and greater surface roughness, while maintaining consistent etching rates. Notably, the etching rate in MACE was found to be significantly higher than in chemical etching, with particle size identified as the dominant factor influencing etching dynamics. Interestingly, the distribution of particles (random or periodic) had minimal impact on overall etching rates, further underscoring the importance of particle dimensions. Moreover, experimental validation on Au-coated GaAs substrates showed strong agreement between simulated and empirical surface morphologies. Additionally, oxidant concentration was identified as a key parameter modulating etching characteristics, with higher concentrations accelerating chemical reactions and producing more pronounced surface modifications. These findings have significant implications for nanoscale engineering, particularly in applications such as nanoelectronics, photovoltaics, and advanced sensor technologies. The phase-field modeling framework developed in this study provides a powerful computational tool for predicting and optimizing MACE processes, enabling more precise and controlled nanostructure fabrication. Future research should aim to extend the model to different substrate materials, explore complex metal catalyst configurations, and refine numerical parameters for enhanced predictive accuracy. This study provides a robust foundation for advancing MACE techniques and their applications in cutting-edge technological innovations.

ACKNOWLEDGMENT

This work is supported by Ministry of Science and Technology, Republic of China (Taiwan) under grant MOST 111-2221-E-024-010.

REFERENCES

Arafat, M.Y., Islam, M.A., Mahmood, A.W.B., Abdullah, F., Nur-E-Alam, M., Kiong, T.S. and Amin, N. "Fabrication of black silicon via metal-assisted chemical etching-A review," *Sustainability*, Vol. 13, No. 19, 10766 (2021).

Cahn, John W. and Hilliard John E. "Free Energy of a Nonuniform System. I. Interfacial Free Energy," *J. Chem. Phys*., Vol. 28, pp. 258-267 (1958).

Celik, A.N., Tuncel, B., Avishan, N., Shah, S.N. and Hussain, N. "Bottom-up and top-down strategies for fabrication of silicon nanowires," *Mater. Innov*., Vol. 2, No. 3, pp. 69-82 (2022).

DeJarld, M., Shin, J.C., Chern, W., Chanda, D., Balasundaram, K., Rogers, J.A. and Li, X. "Formation of high aspect ratio GaAs nanostructures with metal-assisted chemical etching," *Nano Lett*., Vol. 11, No. 12, pp. 5259-5263 (2011).

Dusheiko, M.G., Koval, V.M. and Obukhova, T.Yu. "Silicon nanowire arrays synthesized using the modified MACE process: Integration into chemical sensors and solar cells," *Semicond. Phys. Quantum Electron. Optoelectron.*, Vol. 25, No. 1, pp. 058-067 (2022).

Eggleston, J.J., McFadden, G.B. and Voorhees, P.W. "A phase-field model for highly anisotropic interfacial energy," *Phys. D: Nonlinear Phenom*., Vol. 150, No. 1-2, pp. 91-103 (2001).

Geng, X., Qi, Z., Li, M., Duan, B.K., Zhao, L. and Bohn, P.W. "Fabrication of antireflective layers on silicon using metal-assisted chemical

etching with in situ deposition of silver nanoparticle catalysts," *Sol. Energy Mater. Sol. Cells*, Vol. 103, pp. 98-107 (2012).

He, C.L., Yang, X.F., Ma, G.F., Wang, J.M., Du, Z.F., Zhao, D.L. and Cai, Q.K. "Fabrication of anti-reflecting silicon surfaces for solar cells using ag assisted chemical etching," *Adv. Mater. Res.*, Vol. 631-632, pp. 717-720 (2013).

Huang, Z., Fang, H. and Zhu, J. "Fabrication of silicon nanowire arrays with controlled diameter, length, and density," *Adv. Mater.,* Vol. 19, No. 5, pp. 744-748 (2007).

Jiang, B., Li, M., Liang, Y., Bai, Y., Song, D., Li, Y. and Luo, J. "Etching anisotropy mechanisms lead to morphology-controlled silicon nanoporous structures by metal assisted chemical etching," *Nanoscale,* Vol. 8, No. 5, pp. 3085-3092 (2016).

Kim, J. "Three-dimensional numerical simulations of a phase-field model for anisotropic interfacial energy," *Commun. Korean Math. Soc*., Vol. 22, No. 3, pp. 453-464 (2007).

Kobayashi, R. "Modeling and numerical simulations of dendritic crystal growth," *Phys. D: Nonlinear Phenom*., Vol. 63, No. 3-4, pp. 410-423 (1993).

Kolasinski, K.W. "Metal-assisted catalytic etching (MACE) for nanofabrication of semiconductor powders," *Micromachines*, Vol. 12, No. 7, 776 (2021).

Kolasinski, K.W., Unger, B.A., Ernst, A.T. and Aindow M. "Crystallographically determined etching and its relevance to the metal-assisted catalytic etching (MACE) of silicon powders," *Front. Chem*., Vol. 6, 651 (2019).

Kong, L., Dasgupta, B., Ren, Y., Mohseni, Parsian K., Hong, M., Li, X. Chim, W.K. and Chiam, S.Y. "Evidences for redox reaction driven charge transfer and mass transport in metal-assisted chemical etching of silicon," *Sci. Rep.*, Vol. 6, 36582 (2016).

Leonardi, A.A., Faro, M.J.L., and Irrera, A. "Silicon Nanowires Synthesis by Metal-Assisted Chemical Etching: A Review," *Nanomater.*, Vol. 11, 383 (2021).

Li, Y., Li, M., Song, D., Liu, H., Jiang, B., Bai, F. and Chu, L. "Broadband light-concentration with near-surface distribution by silver capped silicon nanowire for high-performance solar cells," *Nano Energy*, Vol. 11, pp. 756-764 (2015).

Lin, C., Kim, K., Wang, Z., Yan, Z., Tang, Z. and Liu, Y. "Mace-like TTF-TCNQ/HKUST-1 composite structures for rapid NO_2 detection: Synergistically induced ultrahigh sensitivity and outstanding selectivity," *Nano Res.*, Vol. 16, pp. 13366-13374 (2023).

Liu, H., Du, Y.X., Yin, X.T., Bai, M.Y. and Liu, W.G. "Micro/nanostructures for light trapping in monocrystalline silicon solar cells," *J. Nanomater*., Vol. 2022, No.1, 8139174 (2022).

Mohamedyaseen, A. and Suresh Kumar, P. "The fabrication of high-anisotropy silicon nanowires based on MACE method for photonic sensor," *Silicon*, Vol. 14, pp. 11417-11427 (2022).

Nur'aini, A. and Oh, I. "Deep Etching of Silicon Based on Metal-Assisted Chemical Etching," *ACS Omega*, Vol. 7, pp. 16665-16669 (2022).

Salem, A.M.S., Harraz, Farid A., El-Sheikh, S.M. and Shah, S. Ismat "Novel Si nanostructures via Ag-assisted chemical etching route on single and polycrystalline substrates," *Mater. Sci. Eng. B*, Vol. 262, 114793 (2020).

Shimizu, T., Tanaka, N., Tada, Y., Hara, Y., Nakamura, N., Taniuchi, J., Takase, K., Ito, T. and Shingubara, S. "Fabrication of nanocone arrays by two step metal assisted chemical etching method," *Microelectron. Eng*., Vol. 153, pp. 55-59 (2016).

Stafiniak, A., Prażmowska. J., Macherzyński, W. and Paszkiewicz, R. "Nanostructuring of Si substrates by a metal-assisted chemical etching and dewetting processs," *RSC Adv*., Vol. 8, No. 54, pp. 31224-31230 (2018).

Suo, Z. and Lu, W. "Forces that drive nanoscale self-assembly on solid surfaces," *J. Nanopart. Res*., Vol. 2, pp. 333-344 (2000).

Wu, H. and Cui, Y. "Designing nanostructured Si anodes for high energy lithium ion batteries," *Nano Today*, Vol. 7, No. 5, pp. 414-429 (2012).

Yu, H.-C. and Lu, W. "Dynamics of the self-assembly of nanovoids and nanobubbles in solids," *Acta. Mater*., Vol. 53, No. 6, pp. 1799-1807 (2005).

Zhang, Z.L., Wang, B., Chen, Y., Tang, Y.H., Song, X.M., Li, Q.L. and Yan, H. "Preparation of pyramid-sinws binary structure with ag nanoparticles-assisted chemical etching," *Rare Met*., Vol. 38, No. 4, pp. 312-315 (2019).